Miner Deposita (2018) 53:649–663
https://doi.org/10.1007/s00126-017-0768-y

ARTICLE

Melt recharge, f_{O2}-T conditions, and metal fertility of felsic magmas: zircon trace element chemistry of Cu-Au porphyries in the Sanjiang orogenic belt, southwest China

Xuyang Meng[1] · Jingwen Mao[2] · Changqing Zhang[2] · Dongyang Zhang[3] · Huan Liu[2]

Received: 31 August 2017 / Accepted: 1 October 2017 / Published online: 13 October 2017

Abstract The magmatic hydrothermal Pulang Cu deposit (Triassic) and the Beiya Au-Cu deposits (Eocene) are located in the Sanjiang copper porphyry belt, southwest China. Zircon chemistry was used to constrain the magmatic evolution and oxidation state of the porphyries. The results show that porphyries of the Beiya district formed from an early oxidized melt and a later relatively reduced and more evolved magma, whereas Pulang experienced a normal Cu porphyry evolutionary trend. The Pulang porphyries crystallized from more oxidized magma (ΔFMQ + 2.9–4.6, average = 4.0 ± 1.0, *n* = 3) with an average temperature of 709 ± 6 °C compared to the Beiya porphyries (ΔFMQ + 0.6–3.5, average = 1.9 ± 1.3, *n* = 5) with a mean magmatic temperature of 780 ± 22 °C. These data, combined with data from other Cu- and Au-rich porphyries in the Sanjiang belt (i.e., Machangjing Cu, Yao'an Au), are consistent with previous experimental work showing that elevated Cu and Au solubilities in magma require oxidizing conditions. A compilation of existing geochemical data for magmatic zircons from fertile and barren porphyry systems worldwide establishes an optimal diagnostic interval on Ce^{IV}/Ce^{III}-$T_{Ti\text{-}in\text{-}zircon}$ and $(Eu/Eu^*)_N$ plots for generating magmatic hydrothermal Cu-Au deposits.

Keywords Sanjiang orogenic belt · Porphyry-related Cu-Au deposits · Magma recharge · Magmatic redox state

Introduction

Cooling of sulfur-rich oxidized hydrous magma and exsolution of hydrothermal fluids in the middle to upper crust are the primary controls on porphyry Cu-Au systems (Burnham 1980; Blevin and Chappell 1992; Hedenquist and Lowenstern 1994). The solubility of Cu and Au in hydrous silicate melts was proven to be affected by the amount and proportion of dissolved sulfate and sulfide in S-bearing magma, whereas oxygen fugacity controls the speciation of sulfur (Barnes 1979; Hamlyn et al. 1985; Bornhorst and Rose 1986; Jugo 2004; Jugo et al. 2005). The magma oxidation state can be constrained by empirical redox proxies (Soloview 2015). Typical methodologies, such as whole-rock Fe^{3+}/Fe^{2+} ratio measurements (Brett and Sato 1984), amphibole oxygen thermobarometry (Scaillet and Evans 1999; Ridolfi et al. 2010; Ridolfi and Renzulli 2012), and ilmenite-magnetite oxygen thermobarometry (Buddington and Lindsley 1964; Ghiorso and Sack 1991; Lepage 2003), are all adequate in evaluating the magmatic redox state of unaltered intrusive rocks. However, hydrothermal alteration and magmatic hydrothermal ore formation invariably affect the primary texture and bulk-rock chemistry of Cu-Au porphyry intrusions and may conceal the original igneous rock signature. Accessory minerals such as zircon can better retain the primary chemical information due to slow growth and dissolution (Watson 1996) and low intracrystalline diffusivities (Cherniak et al.

Editorial handling: B. Lehmann

Electronic supplementary material The online version of this article (https://doi.org/10.1007/s00126-017-0768-y) contains supplementary material, which is available to authorized users.

✉ Jingwen Mao
jingwenmao@263.net

[1] School of Earth Sciences and Resources, China University of Geosciences, Beijing 100083, China

[2] MLR Key Laboratory of Metallogeny and Mineral Assessment, Institute of Mineral Resources, Chinese Academy of Geological Sciences, Beijing 100037, China

[3] State Key Laboratory of Geological Processes and Mineral Resources, China University of Geosciences, Wuhan 430074, China

1997). Thus, chemically stable zircon populations are well suited to record the evolution of a magmatic system, and the associated fluctuations in f_{O2}-T conditions.

The Sanjiang orogenic belt in southwest China hosts several large Cu-Au porphyry deposits that formed in distinct tectonic settings (Mao et al. 2014). These include the subduction-related Triassic Pulang porphyry Cu deposit in the Zhongdian arc (the southern part of Yidun arc), and the post-collisional Tertiary Beiya porphyry-skarn Au-Cu deposits within a potassic igneous belt along the Ailaoshan-Red River shear zone. The two deposits are the focus of our study. We attempt to evaluate the f_{O2}-T conditions and magma evolution through the trace element concentration of zircons that crystallized in the two porphyries. We then compare these data with other published global data to propose a discrimination diagram for ore-bearing and ore-barren porphyries.

Geological background

Yidun arc

The NNW-trending Yidun arc is surrounded by the Qiangtang terrane to the west, Songpan-Garze fold belt to the northeast, and Yangtze craton to the southeast, respectively. The Garze-Litang and Jinshajiang suture zones lie to the east and west of the Yidun arc, respectively (Fig. 1). The Zhongza massif in the western part of the Yindun arc, divided by the NS-trending Xiangcheng-Geza fault, comprises carbonate-dominated Paleozoic metasedimentary rocks intercalated with mafic volcanic rocks. It is suggested to have been separated from the western Yangtze craton by opening of the Garze-Litang Ocean in the Late Permian (Chen et al. 1987; Chang 1997; Hou et al. 2003). In contrast, the eastern Yidun arc is dominated by Late Triassic volcano-sedimentary successions consisting of flysch and mafic-felsic arc-related volcanic rocks (BGMRSP 1991). The Late Triassic through Miocene dioritic-granitic plutons extend for more than 500 km from north to south, and become progressively younger towards the east (BGMRSP 1991; Hou et al. 2003).

The Yidun arc underwent three main tectonic, magmatic, and metallogenic events during Triassic subduction of oceanic crust, Jurassic-Cretaceous collision, and post-collision, and then affected by Cenozoic intracontinental strike-slip shearing and convergence (Mo et al. 1993; Li et al. 2011; Deng et al. 2014). A continuous glaucophane schist belt (Sha 1998) and an ophiolitic suite along the suture zone (Zeng et al. 2004) are products of the subduction. The NW-oriented Triassic stocks and dikes comprise hypabyssal quartz diorite porphyry, quartz monzonite porphyry, and granite porphyry. Some of these are the causative intrusions for Cu ± Mo ± Au mineralization. These adakite-like calc-alkaline porphyries (e.g., Pulang, Xuejiping, and Langdu) resulted from the Triassic westward-dipping subduction of the Garze-Litang Ocean below the Yidun arc (Pan et al. 2003; Li et al. 2011; Wang et al. 2014a). The collision between the Yidun arc and the Yangtze craton took place in the Jurassic and Cretaceous following final closure of the Garze-Litang Ocean. The Late Cretaceous A-type granites in the northern Yidun arc are associated with W-Sn mineralization, whereas Cu-Mo mineralization is mainly related to the coeval magmatism in the southern Yidun arc. The Late Cretaceous magmatism in the southern Yidun arc formed in a post-subduction setting. However, different viewpoints on the controls of the magmatism include the collision between the Lhasa and Qiangtang terranes (Wang et al. 2014b; Peng et al. 2014) or lithospheric-scale transtensional faulting within the Yidun arc (Yang et al. 2015) during Late Cretaceous.

Jinshajiang-Ailaoshan shear zone

Lateral tectonic escape caused by the collision between India and Asia resulted in the formation of the Ailaoshan-Red River shear zone in Paleocene (Tapponnier et al. 1990; Leloup et al. 1995; Yin and Harrison 2000). Strike-slip motion on the shear associated with lithospheric extension resulted in the emplacement of the Eocene-Oligocene alkaline magmatic belt that is 2000-km long and 50–80-km wide (Chung et al. 2005). Contemporaneously, formation of a series of Tertiary rift basins across the Qiangtang terrane and the western Yangtze craton, extrusion of alkaline basalt, and development of a positive gravity anomaly pattern along the Jinshajiang-Red River fault system took place. These formed in a post-collisional extensional setting (Zhang et al. 1987; Turner et al. 1996; Deng et al. 2010), or transpressional setting during continental subduction (Wang et al. 2001) that possibly corresponded to the opening of the South China Sea (Leloup and Kienast 1993; Liang et al. 2007). The Eocene-Oligocene alkaline-rich intrusions are associated with many porphyry and skarn Au-Cu deposits (Hu et al. 2004; Xu et al. 2007; Lu et al. 2013; Tran et al. 2014). Three typical porphyry suites (Beiya, Yao'an, and Machangqing) are located to the east of Jinshajiang suture, which marks the closure of the Jinshajiang Ocean in the Late Triassic (Mo et al. 1993), whereas the Eocene Yulong porphyry copper belt is located to the west along the Jinshajiang suture.

Deposit geology

Pulang Cu deposit

The Pulang Cu deposit (99° 59′ 23″ E, 28° 02′ 19″ N, elevation 3500–4600 m) is hosted by a series of Late Triassic subvolcanic intrusions emplaced into the Late Triassic clastic rocks and andesite of the Tumugou Formation (Figs. 2a and 3). The deposit

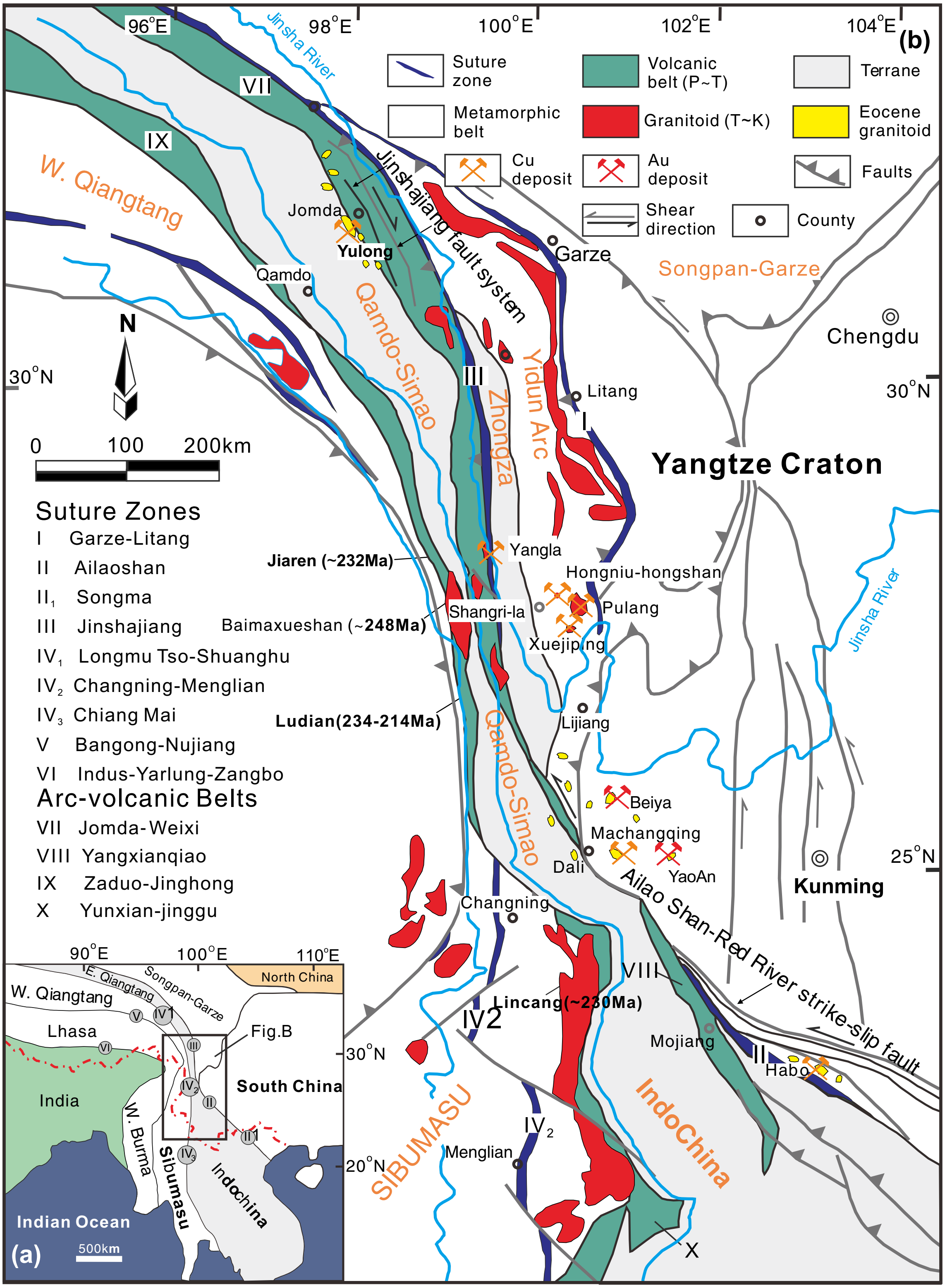

Fig. 1 (**a**) Geological map showing the distribution of major continental blocks and sutures in southeast Asia (Metcalfe 2006; Metcalfe 2013). (**b**) Tectonic framework of the Sanjiang domain in southwest China, showing the major terranes, suture zones, volcanic arcs, and location of the Pulang porphyry Cu-Au deposit and the Beiya porphyry-skarn Au-Cu district (Zi et al. 2012; Deng et al. 2014). Original figure from Zhu et al. (2015), and with publication permission from Economic Geology

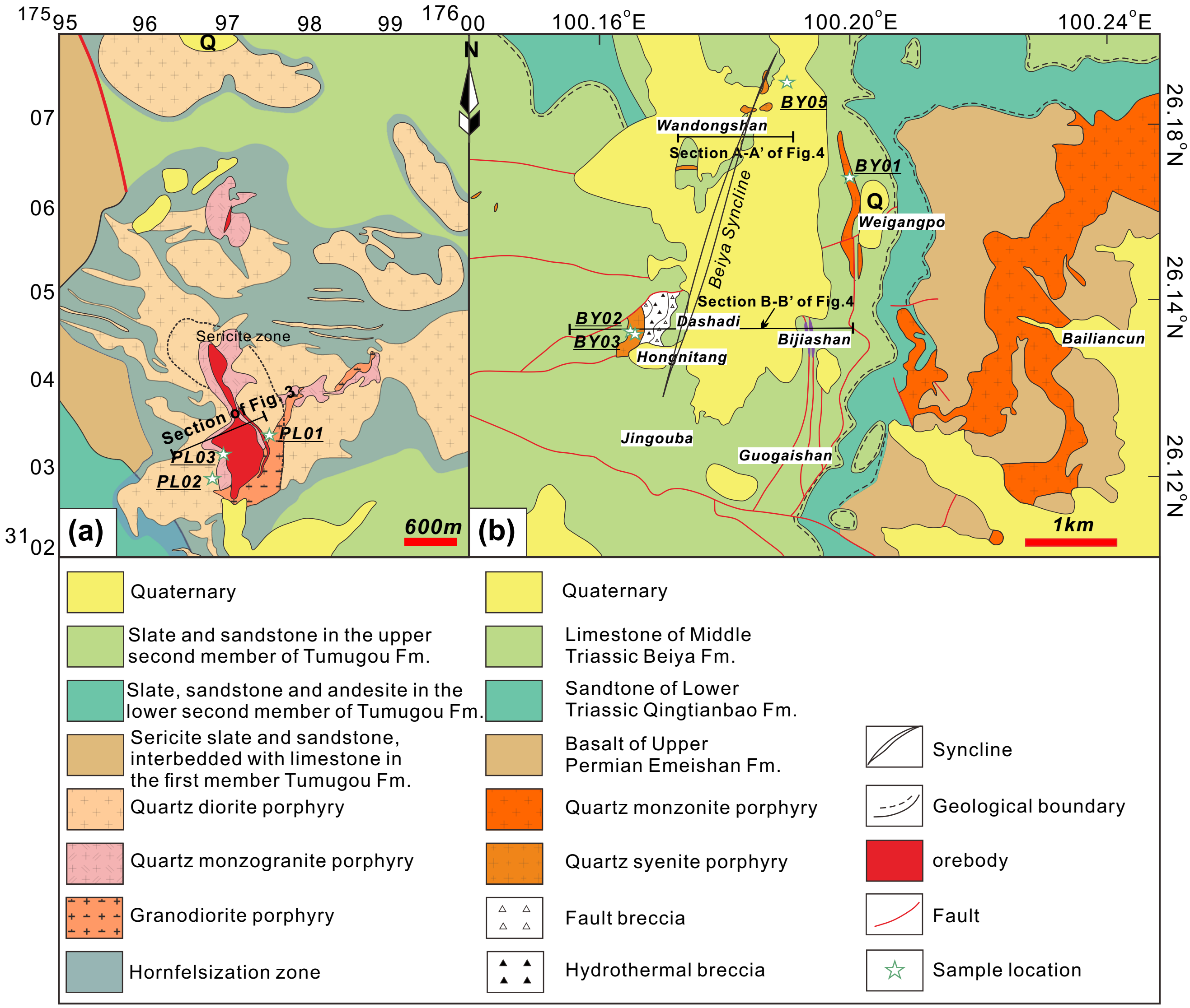

Fig. 2 Simplified geological map of the Pulang deposit area (**a**) and the Beiya district area (**b**) showing the distribution of felsic intrusive phases and the orebodies, modified from Li et al. (2011) and Yunnan Gold & Mineral Group Co., Ltd (2011), respectively. Pentagram represents the sampling location. Sample BY04 was collected outside Fig. 2b

contains inferred reserves of 1.3 Gt with an average grade of 0.34% Cu, 0.18 g/t Au, and 1.27 g/t Ag (Li et al. 2011). It is locally controlled by NW-trending faults. The Pulang igneous stocks comprise of quartz diorite, quartz monzonite, granodiorite, and minor monzodiorite covering an area of 8.9 km^2.

Mineralization in the Pulang porphyry deposit is genetically associated with both quartz diorite porphyry and quartz monzonite porphyry (228–212 Ma) (Wang et al. 2008; Pang et al. 2009; Liu et al. 2013). The quartz diorite porphyry is the most abundant rock and forms nearly 80% of the suite. The rock is gray in color and exhibits a phaneritic matrix of plagioclase (65%), quartz (5%), hornblende (< 1%), and minor K-feldspar, with phenocrysts of plagioclase (25%) and hornblende (< 5%). Phyllic and propylitic alteration are present. The quartz monzonite porphyry forms 20% of the suite. The rock is gray with a phaneritic groundmass of oligoclase (25%), K-feldspar (25%), quartz (15%), and biotite (5%), and phenocrysts of plagioclase (15%), K-feldspar (10%), biotite (5%), and minor quartz. Phyllic, potassic, and silicic alteration are present. A post-mineral granodiorite porphyry dike cuts the quartz monzonite porphyry dike. The granodiorite porphyry contains phenocrysts of plagioclase, K-feldspar, biotite, quartz, and hornblende in a matrix of plagioclase, quartz, hornblende (15%), and biotite (5%). The orebodies are mainly within the phyllic and potassic alteration zones which are superimposed on the quartz monzonite porphyry and the quartz diorite porphyry (Fig. 3). Disseminated, veinlet, and breccia-related mineralization developed. A detailed petrographical description is available in Liu et al. (2015b) and Li et al. (2011).

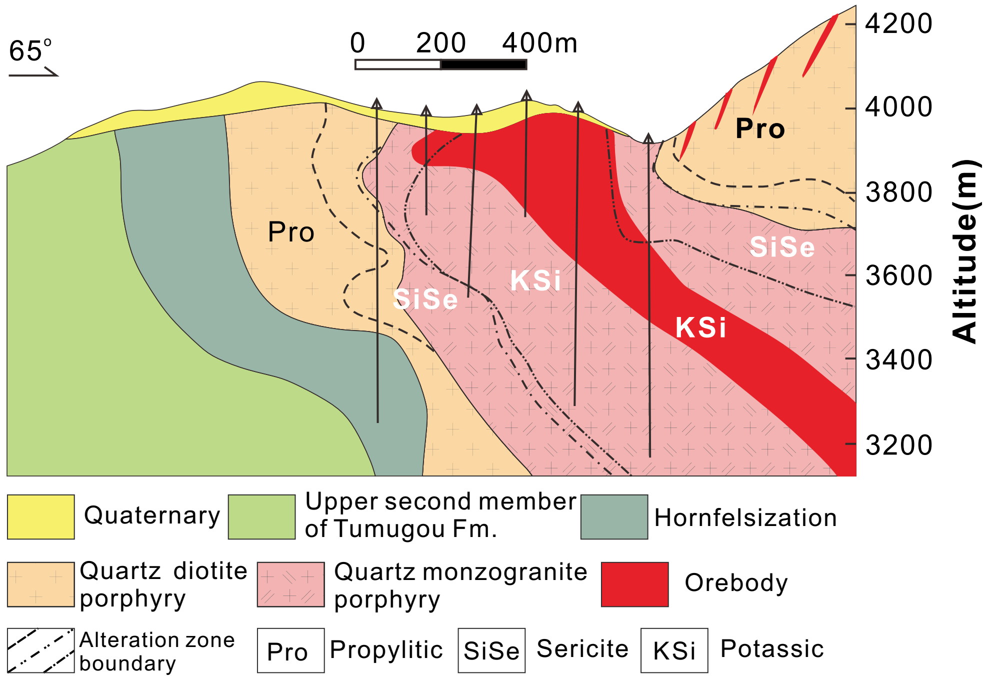

Fig. 3 Southwest-northeast cross section 4 (modified from Li et al. 2011) showing lithological units and the spatial relationship of alteration at the Pulang porphyry copper deposit. Location is shown in Fig. 2a

Beiya Au-Cu district

The Beiya Au-Fe-Cu porphyry and skarn district (100° 08′ 38″ E, 26° 07′ 43″ N, elevation 1700–1900 m) is spatially and temporally associated with several small and buried Eocene-Oligocene potassic porphyritic intrusions covering a total area of 0.34 km^2 (Figs. 2b and 4). The estimated ore reserves are 130 Mt at a grade of 2.42 g/t Au, 0.48% Cu, 25.5% Fe, 38.85 g/t Ag, 1.24% Pb, and 0.53% Zn (He et al. 2016). The Beiya ore district is located along the limbs of the N-S-trending Beiya syncline. It mainly consists of two mineralized zones, with the Wandongshan, Hongnitang, and Dashadi deposits on the west limb of the syncline, and the Weiganpo and Bijiashan zones on the east limb. The peripheral Matouwan and Bailiancun deposits occur in the periphery of the district. The Wandongshan deposit is the currently the location of the main workings and is developed by an open pit (Figs. 2b and 4b). It yields supergene Au ores that were weathered and leached from the hypogene porphyry and skarn ores. Hypogene mineralization is primarily manifested as skarn-type, with subordinate porphyry, fracture-controlled, and quartz (ankerite)-sulfide types (Mao et al. 2017; Xu et al. 2007a).

The country rocks in the Beiya district include ca. 260 Ma flood basalts (Xu et al. 2001) of the Upper Permian Emeishan Formation, sandstones and hornfels of the Lower Triassic Qingtianbao Formation, and limestones of the Middle Triassic Beiya Formation (He et al. 2015). The contact zone between the Triassic limestone and alkaline porphyries is the main host for the metalliferous skarn (Fig. 4). Hydrothermal breccia associated with Au-Fe-Cu mineralization is also present at the Hongnitang deposit. The period of this igneous activity is coeval with regional potassic mafic magmatism in the western part of Yunnan province (37–34 Ma; Lu et al. 2013; Deng et al. 2015; He et al. 2015; Liu et al. 2015a).

The Tertiary intrusions in the Beiya district comprise volumetrically abundant quartz monzonite porphyry and quartz syenite porphyry stocks (37.0–34.6 Ma, LA-ICP-MS zircon U-Pb), granite porphyry (36.6–34.7 Ma, LA-ICP-MS zircon U-Pb), and post-mineralization lamprophyre dikes (Deng et al. 2015; Liu et al. 2015a). The porphyry and skarn mineralization is associated with the quartz monzonite and quartz syenite porphyries (Table 1, Fig. 4). The quartz monzonite porphyry at the Dashadi deposit is light gray and porphyritic, with phenocrysts of K-feldspar (30–35%), plagioclase (20–25%), and minor quartz in a groundmass of K-feldspar and quartz. The quartz monzonite porphyry at the Weiganpo, Bailiancun, and Matouwan deposits has high contents of biotite and amphibole phenocrysts. The quartz syenite porphyries at the Wandongshan, Hongnitang, and Bijiahan deposits are gray-white in color and microgranular and porphyritic, with phenocrysts of K-feldspar (35–45%), quartz (5–10%), and minor plagioclase, and a groundmass of K-feldspar and quartz. The main rock phases are described in Liu et al. (2015a). Subordinate porphyry-type disseminated and vein-type Au-Cu mineralization is typically hosted within fractures and small shears (Mao et al. 2017). Pervasive potassic alteration overprinted the intrusions, altering plagioclase to K-feldspar. Silification, and phyllic and propylitic alteration also occur. Overall, porphyry mineralization within these stocks is weak and they lack typical alteration zoning.

The granite porphyry intrusion hosts porphyry-type mineralization with abundant Au-rich pyrite and subordinate

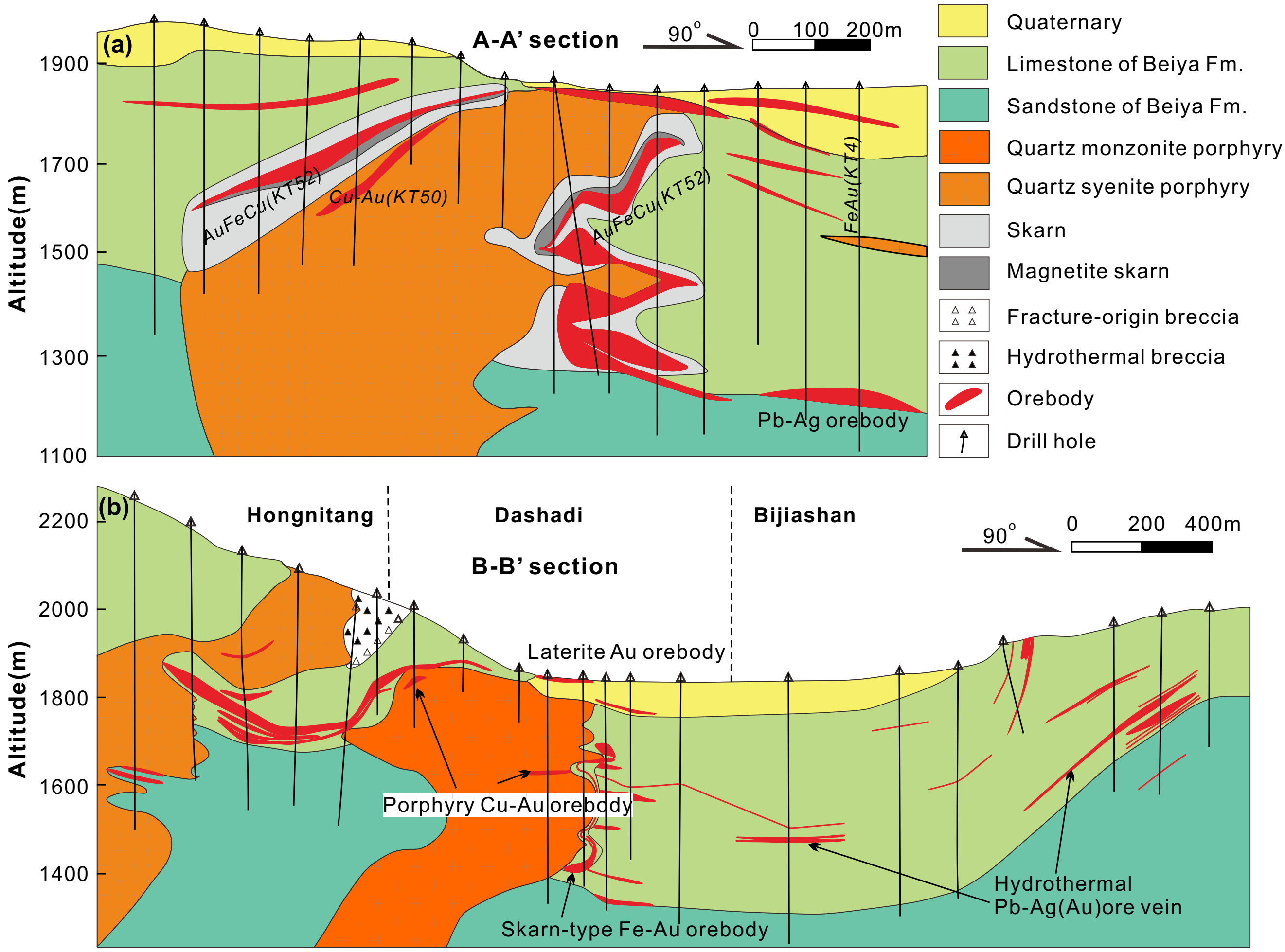

Fig. 4 West-east cross section A-A′ and B-B′ (modified after YunNan Gold & Mineral Group Co., 2011) showing lithological units and the spatial relationship of mineralization assemblages of the Beiya district. Location is shown in Fig. 2b

chalcopyrite, galena, and other sulfides. Potassic and phyllic alteration has also overprinted the intrusion. The mineralization in the granite porphyry is roughly synchronous with the other porphyry and skarn mineralization in this district (Deng et al. 2015; Liu et al. 2015a). The vein-type pyrite within the granite porphyry intrusions has a higher Au content (1–10 ppm) than the pyrite (0.01–1 ppm Au) from the Fe-Au orebodies and skarn in limestone associated with porphyritic

Table 1 Mineralogy and location of porphyry samples from Pulang Cu deposit and Beiya Au-Cu district in the Sanjiang orogenic belt

Sample	Deposit	Location	Lithology	Primary mineralogy		Alteration
				Phenocrysts	Groundmass	
PL01	Pulang	X17597658, Y3103360	QDP	Pl, Amp	Pl, Qtz, Amp, Kfs	Phyllic, propyllic,
PL02	Pulang	ZK713, 567.5 m	QDP	Pl, Amp	Pl, Qtz, Amp, Kfs	Phyllic, propyllic,
PL03	Pulang	ZK416, 172.5 m	QMP	Pl, Kfs, Bi, Qtz	Pl, Kfs, Qtz, Bi	Phyllic, potassic
BY01	Beiya	Weiganpo	QMP	Kfs, Pl, Bt	Kfs, Qtz	Argillic, potassic, phyllic
BY02	Beiya	Hongnitang	QSP	Kfs, Qtz, Pl	Kfs, Qtz	Argillic, potassic, phyllic
BY03	Beiya	Hongnitang	QSP	Kfs, Qtz, Pl	Kfs, Qtz	Argillic, potassic, phyllic
BY04	Beiya	Matouwan	QMP	Pl, Kfs, Amp, Bt, Qtz	Kfs, Qtz	Argillic, potassic, phyllic
BY05	Beiya	Wandongshan	QSP	Kfs, Qtz, Pl	Kfs, Qtz	Argillic, potassic, phyllic

QDP, quartz diorite porphyry; *QMP*, quartz monzonite porphyry; *QSP*, quartz syenite porphyry; *Kfs*, K-feldspar; *Qtz*, quartz; *Pl*, plagioclase; *Bt*, biotite; *Amp*, amphibole monzogranite (Deng et al. 2015). These two magma pulses share similar geochemical and isotopic signatures to the amphibole xenoliths in the potassic felsic intrusions in the western part of Yunnan province, suggesting an origin from K-rich thickened lower crust during the melting of metasomatized subcontinental lithospheric mantle (Deng et al. 2015; Liu et al. 2015a).

Sample preparation and analytical methods

Samples from the quartz diorite porphyry (PL01, PL02) and quartz monzonite porphyry (PL03) at the Pulang deposit, and quartz monzonite porphyry (BY01, BY04) and quartz syenite porphyry (BY02, BY03, BY05) in the Beiya district were prepared for zircon separation. Zircon separation was conducted by conventional heavy liquid and magnetic separation techniques. Representative grains were handpicked and mounted in epoxy resin, and then polished to reveal their internal structures. Reflected and transmitted light photomicrographs were examined for all zircons, as were cathodoluminescence (CL) scanning electron microscope images, to identify the internal structure of zircons and ensure that the laser ablation analytical points were wholly within the rim or the core. The xenocrystic zircons in the Beiya porphyries (Deng et al. 2015) are characterized by partially overgrown clear core-rim structures, or by corroded textures. Such crystals were carefully removed prior to analysis. Most zircons were previously prepared for laser ablation inductively coupled plasma mass spectrometry (LA-ICP-MS) U-Pb dating (not reported here) to exclude inherited zircons. Where possible, if the zircon crystal was large enough, multiple analyses were conducted on single grains to evaluate core-to-rim chemical variation. Additionally, melt inclusions and fractures were avoided during the laser ablation analyses of zircons according to details from the CL images. The measured P, Ca, Sr, and Al contents of zircons were also used to monitor sub-surface inclusions. In this study, most zircon analyses have very low P, Ca, Sr, and Al concentrations.

Trace elements, including rare earth element (REE) contents of the zircons, were determined by LA-ICP-MS at the National Research Center of Geoanalysis in Beijing, China. The LA-ICP-MS analyses used a Finnigan MAT ELEMENT II high-solution inductively coupled plasma spectrometer (HR-ICP-MS) with a

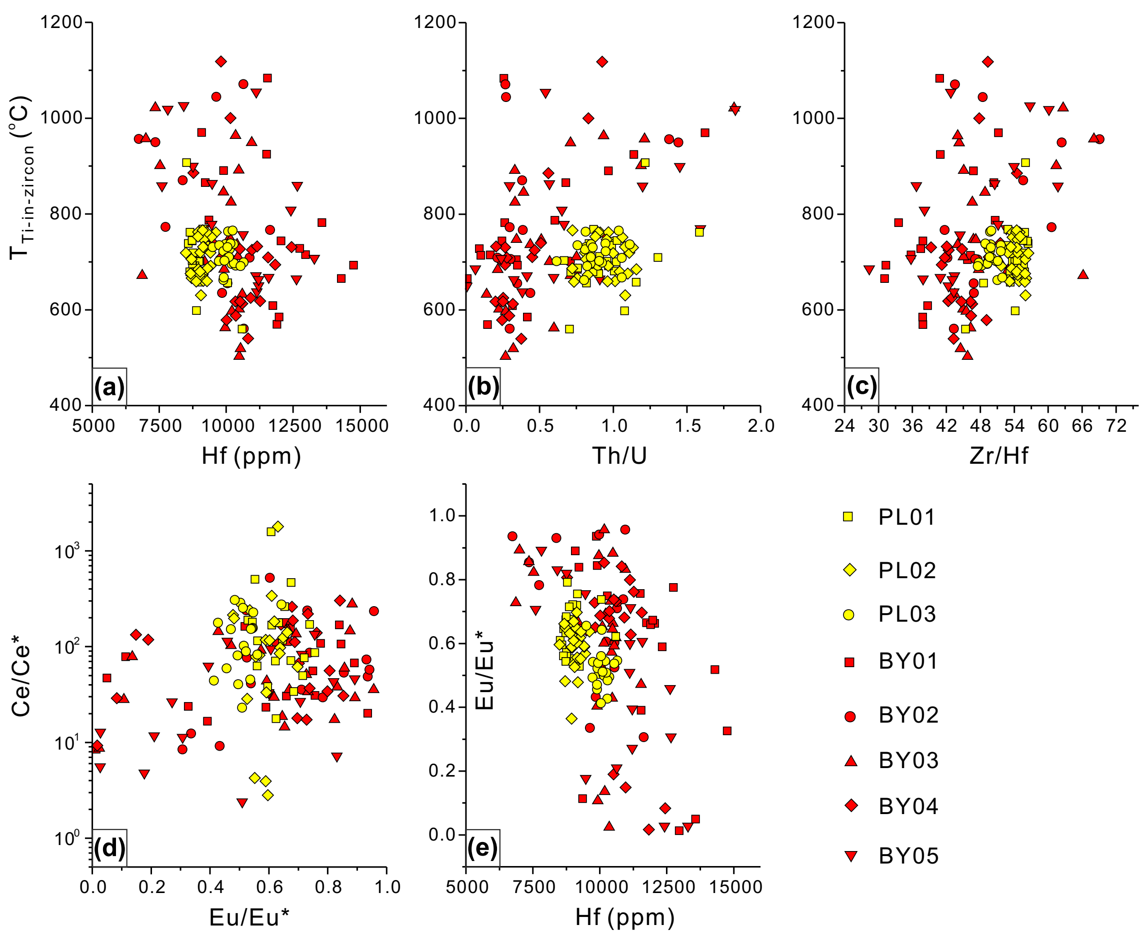

Fig. 5 Trace element variation diagrams for the studied zircons. **a** $T_{Ti\text{-}in\text{-}zircon}$ vs. Hf. **b** $T_{Ti\text{-}in\text{-}zircon}$ vs. Th/U. **c** $T_{Ti\text{-}in\text{-}zircon}$ vs. Zr/Hf. **d** Ce/Ce* vs. Eu/Eu*. **e** Eu/Eu* vs. Hf

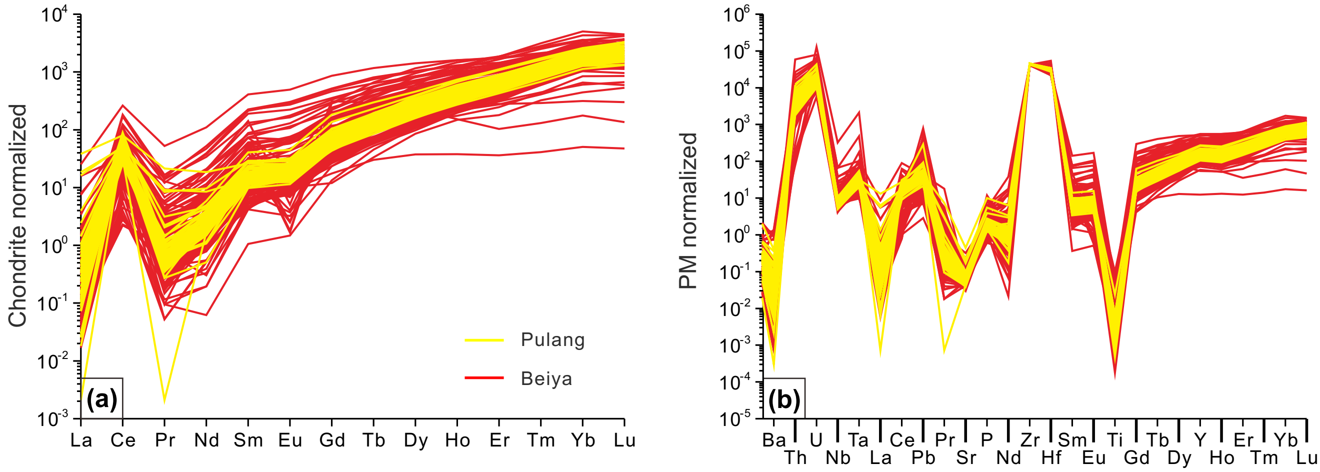

Fig. 6 Chondrite-normalized rare earth element (REE) patterns (**a**) and primitive mantle-normalized trace element diagrams (**b**) for zircons from the Pulang and Beiya porphyry stocks. Normalization values are from Sun and McDonough (1989)

high-performance interface coupled with a New-Wave UP-193nm Nd: YAG UV laser. Ablation was carried out by a He-Ar gas mixture (flow rate of 0.73 L He/min and 0.85 L Ar/min) and the resulting vapor was combined with argon before delivery into the ICP-MS. The analyses were conducted using a 35-μm spot diameter, a 10-Hz frequency, a 0.25-mJ/pulse power, during a 70-s analysis including 20 s measurement of gas blank, followed by ablation of the sample for approximately 40 s by raster. Each group of ten zircon analyses was bracketed by analysis of standard glass NIST612, NIST 610, and Kl2g to correct for mass bias drift during analysis. The calibration procedure using internal standards and matrix normalization followed Hu et al. (2011). The full data set for minor and trace elements obtained by LA-ICP-MS is provided as ESM I. The f_{O2}-T calculation methods are documented in the ESM II, in which f_{O2} is calculated through the La-Pr interpolation method. The Ce^{IV}/Ce^{III} ratio is estimated through the lattice-strain model that was extensively used in previous studies.

Results

Trace elements

Zircons from the Pulang and Beiya porphyries have Hf concentrations ranging from 8500 to 10,700 ppm and 6900 to 16,700 ppm, respectively (Fig. 5a). Similar to other studies of felsic stocks (Claiborne et al. 2010; Dilles et al. 2015), the hafnium content decreases, and Zr/Hf and Th/U ratios of zircon increase with declining Ti-in-zircon model crystallization temperature (Fig. 5a–c). Zircons in the studied fertile porphyries typically exhibit low light REE and elevated heavy REE contents, with distinctive positive Ce but comparable negative Eu anomalies (Fig. 6). The zircon Ce anomalies of the Pulang porphyries are comparable to those of the Beiya porphyries (Fig. 5d, e). The Eu anomalies are modest and similar among the porphyries, yielding average values between 0.5 and 0.7, but a small proportion of zircons from the Beiya porphyries exhibits lower negative Eu anomalies than the Pulang porphyries (Fig. 6).

Estimates of magmatic oxidation state by different methods

The estimated ΔFMQ values (La-Pr interpolation) of the Pulang porphyries are 2.9–4.6 (average = 4.0 ± 1.0, n = 3) which are slightly higher than those of the Beiya porphyries (0.6–3.5, average = 1.9 ± 1.3, n = 5), but are comparable with

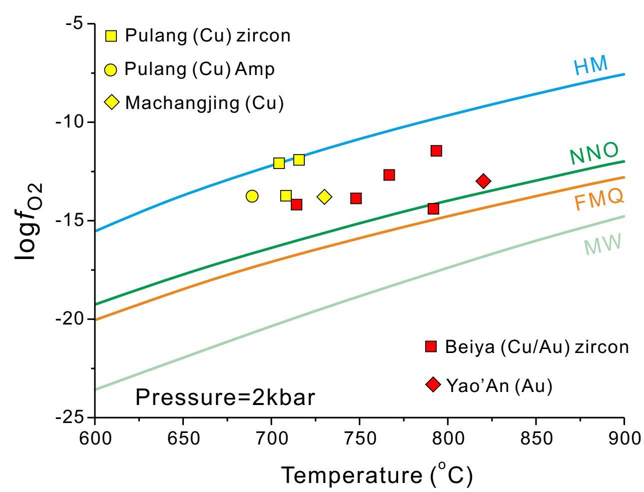

Fig. 7 Plot of oxidation state and temperature (logf_{O2} vs. temperature, at 2 kbar pressure). The points represent average values of each sample in this study or results from the literature. The oxygen fugacities of the Pulang Cu, Machangqing Cu, and Yao'an Au porphyries are compiled for comparison; these values are calculated using the data from Liu et al. (2013) and Bi et al. (2009). *FMQ* fayalite-magnetite-quartz buffer curve (Huebner 1971), *HM* hematite-magnetite buffer curve (≈FMQ + 5; Chou 1978), *MW* wüstite-magnetite buffer curve (Eugster and Wones 1962), *NNO* nickel-nickel oxide buffer curve (≈FMQ + 0.7; Huebner and Sato 1970)

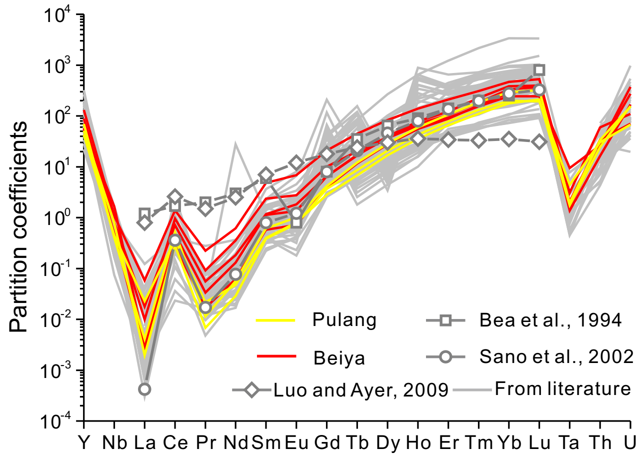

Fig. 8 Diagrams illustrating the zircon/rock partition coefficients (*D*) obtained in this study. The gray lines represent the zircons from previous literature (Xin and Qu 2008; Lee 2008; Peytcheva et al. 2009; Guo et al. 2011; Luo et al. 2011; Wainwright et al. 2011; Wang et al. 2012; Simmons 2013; Farmer 2013). Comparative experimental values (zircon/melt partition coefficients) are represented by squares (Bea et al. 1994), circles (Sano et al. 2002), and diamonds (Luo and Ayers 2009). See data in ESM III

the results obtained in the published amphibole chemistry (Fig. 7). Our results for the Beiya porphyries resemble those calculated from amphibole chemistry (NNO + 1.7, 660–805 °C; W. Y. He, oral commun., February 24, 2017).

Discussion

Zircon/rock partition coefficients

The ratios of rare element concentrations in zircons versus those of the host rocks are compared with the experimental and natural partition coefficients from previous studies (Fig. 8). The obtained average zircon/rock partition coefficients of the studied porphyry samples are consistent with the $D_{zircon/melt}$ value of Sano et al. (2002) but slightly higher than the $D_{zircon/rock}$ from other studies (Rubatto and Hermann 2007; Hanchar and Van Westrenen 2007; Luo and Ayers 2009). As discussed in Claiborne et al. (2006), Hanchar and Van Westrenen (2007), and Nardi et al. (2013), the estimated REE patterns calculated through $D_{zircon/melt}$ values of Sano et al. (2002) and zircon REE compositions are consistent with the whole-rock REE patterns, indicating the behavior of trace elements in the melt is predictable from partition coefficient mineral/melt (Fujimaki 1986; Green 1994; Luo and Ayers 2009). The consistency of our $D_{zircon/rock}$ values with Sano et al. (2002) may suggest that the whole-rock composition reflects the composition of the magma from which it crystallized. To support this suggestion, we use the calculated average $D_{zircon/rock}$ values of the zircon populations from the published literature for comparison and obtain a good agreement (Fig. 8, ESM-III and reference in). One may argue that the zircon grains could crystallize late during the solidification of felsic magmas, thereby reducing the validity of whole-rock REE values as melt REE composition. However, the phosphorus contents of the studied porphyries are low (< 0.5 wt%), indicating that the effects of other REE-bearing minerals (e.g., apatite and monazite, which are early crystallization phases in magma) on bulk composition should be limited. This result also suggests that the REE elements are mostly controlled by zircon structure and are little affected by undetected mineral inclusions. We thus propose that the melt composition mainly determines the rare element contents in the studied zircons.

Table 2 Ti-in-zircon temperature, Ce^{IV}/Ce^{III} (lattice-strain model) and f_{O2} (La-Pr interpolation) values calculated using zircon chemistry

Samples	Ti-in-zircon temperature (°C)	10,000/T (K)	Ce^{IV}/Ce^{III}	lg(f_{O2})	δFMQ
PL01	704.3	10.2	405.6	−12.1	4.6
PL02	708.1	10.2	407.4	−13.7	2.9
PL03	715.5	10.1	383.3	−11.9	4.6
Average	709.3	10.2	398.7	−12.6	4.0
1σ	5.7	0.1	13.4	1.0	1.0
BY01	766.6	9.6	253.1	−12.7	2.9
BY02	793.3	9.4	412.5	−11.5	3.5
BY03	791.7	9.4	371.4	−14.4	0.6
BY04	747.8	9.8	268.1	−13.9	2.0
BY05	799.6	9.3	190.0	−11.9	0.6
Average	779.8	9.5	299	−12.9	1.9
1σ	22	0.2	91	1.3	1.3

The f_{O2} and δFMQ are calculated through La-Pr interpolation methods, whereas the Ce^{IV}/Ce^{III} ratios are estimated based on lattice strain model for comparison with other literature. The detailed discussion of the calculation methods is shown in Digital Supplement II

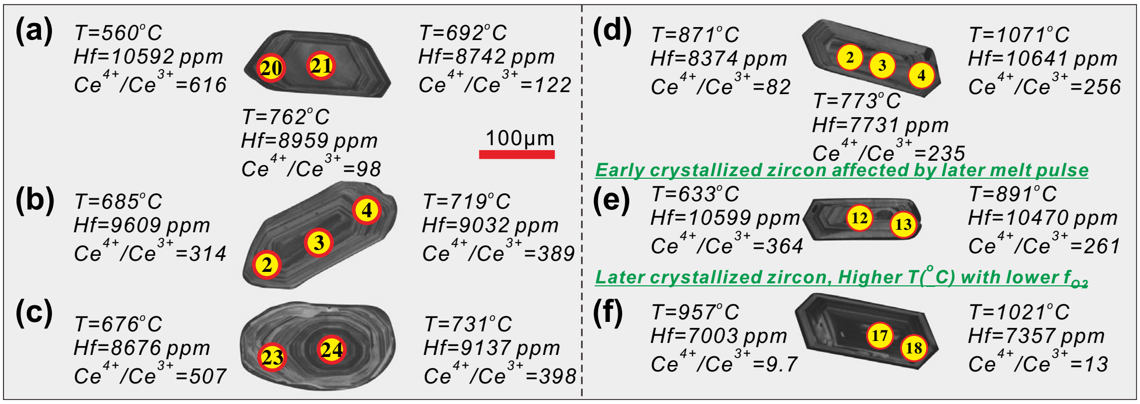

Fig. 9 Cathodoluminescence images of several representative large zoned zircons from the Pulang (**a–c**) and Beiya (**d–f**) porphyry stocks showing LA-ICP-MS spots and corresponding trace element data. T (°C) = temperature (Ti-in-zircon)

Zircon as recorder of magmatic evolution

The above discussion provides us insights that the rare element composition of zircon is determined by the composition of the melt coexisting with crystallizing zircon. Using Hf as an indicator of fractionation (Claiborne et al. 2006) and Ti as a proxy for temperature (Ferry and Watson 2007), the rimward decrease of Ti in zircons from the Pulang porphyry samples is consistent with crystallization by oversaturation upon cooling. A systematic decrease in the Zr/Hf ratio and increase in Y, Th, and U concentrations support this conclusion. The Ti-in-zircon temperatures of the Pulang felsic stocks yield a tight range of 704–715 °C, averaging 709 ± 6 °C, whereas those of the Beiya porphyry system exhibit a wider range of 767–793 °C, averaging 780 ± 22 °C (Table 2). The highly variable geochemical parameters (e.g., REE content, Ce^{IV}/Ce^{III}, Ce/Nd, Hf) of zircons from the Beiya porphyries, and opposing zonation patterns in single crystals, argue against a simple magmatic evolution of the Beiya porphyries (Fig. 9, Table 3).

The negative correlation between Ce/Nd and Th/U ratios indicates that zircon fractionation controls Ce content. The Ce^{IV}/Ce^{III} ratio inversely correlates with the Th/U ratio, suggesting that elevated Ce may be impacted by the effects of variable oxygen fugacity. The narrow range of Ce^{IV}/Ce^{III}, Th/U, and Zr/Hf ratios, as well as the Hf concentrations, are expected in an undisturbed oxidized parental magma reservoir. However, the Beiya porphyries seem to crystallize over a wider range of f_{O2} and over a longer time interval (wide range of Hf), and the redox state remains constant or tends to become more reduced with Hf increases above 11,000 ppm (Fig. 10b). The opposite trend of Ce^{IV}/Ce^{III} versus Hf compared to the typical pattern for the Pulang porphyry stock samples indicates that the magma chamber generating the Beiya porphyry intrusions was perturbed.

In summary, the rimward increase of Ti-in-zircon model temperature and decrease of Ce^{IV}/Ce^{III} ratio in the zircon crystals (Fig. 9d–f), and the larger scatter in all geochemical parameters (Fig. 10) for the Beiya porphyries,

Table 3 Representative chemical parameters of core-rim pairs of zircons from Pulang and Beiya porphyries

Analysis no.	Location	T (°C)	Hf (ppm)	Th/U	Zr/Hf	Ce/Nd	Ce^{IV}/Ce^{III}
PL01–20	Rim	560	10,592	0.70	45.4	38.2	616
PL01–21	Core	692	8742	0.89	55.7	11.4	122
PL02–2	Rim	685	9609	1.16	54.9	21.8	314
PL02–3	Core	762	8959	0.97	54.9	6.6	98
PL02–4	Rim	719	9032	1.11	54.6	28.8	389
PL02–23	Rim	676	8676	1.10	55.9	26.4	398
PL02–24	Core	731	9137	1.08	53.4	23.0	507
BY02–2	Core-Rim	871	8374	0.38	55.6	5.0	82
BY02–3	Core	773	7731	0.30	60.6	14.6	235
BY02–4	Rim	1071	10,641	0.27	43.5	12.0	256
BY03–12	Core	633	10,599	0.14	43.5	17.1	364
BY03–13	Rim	891	10,470	0.33	45.1	15.3	261
BY03–17	Core	957	7003	1.21	68.1	3.1	9.7
BY03–18	Rim	1021	7357	1.82	62.7	5.1	13

The calculated model temperatures vary within ±30 °C (2σ)

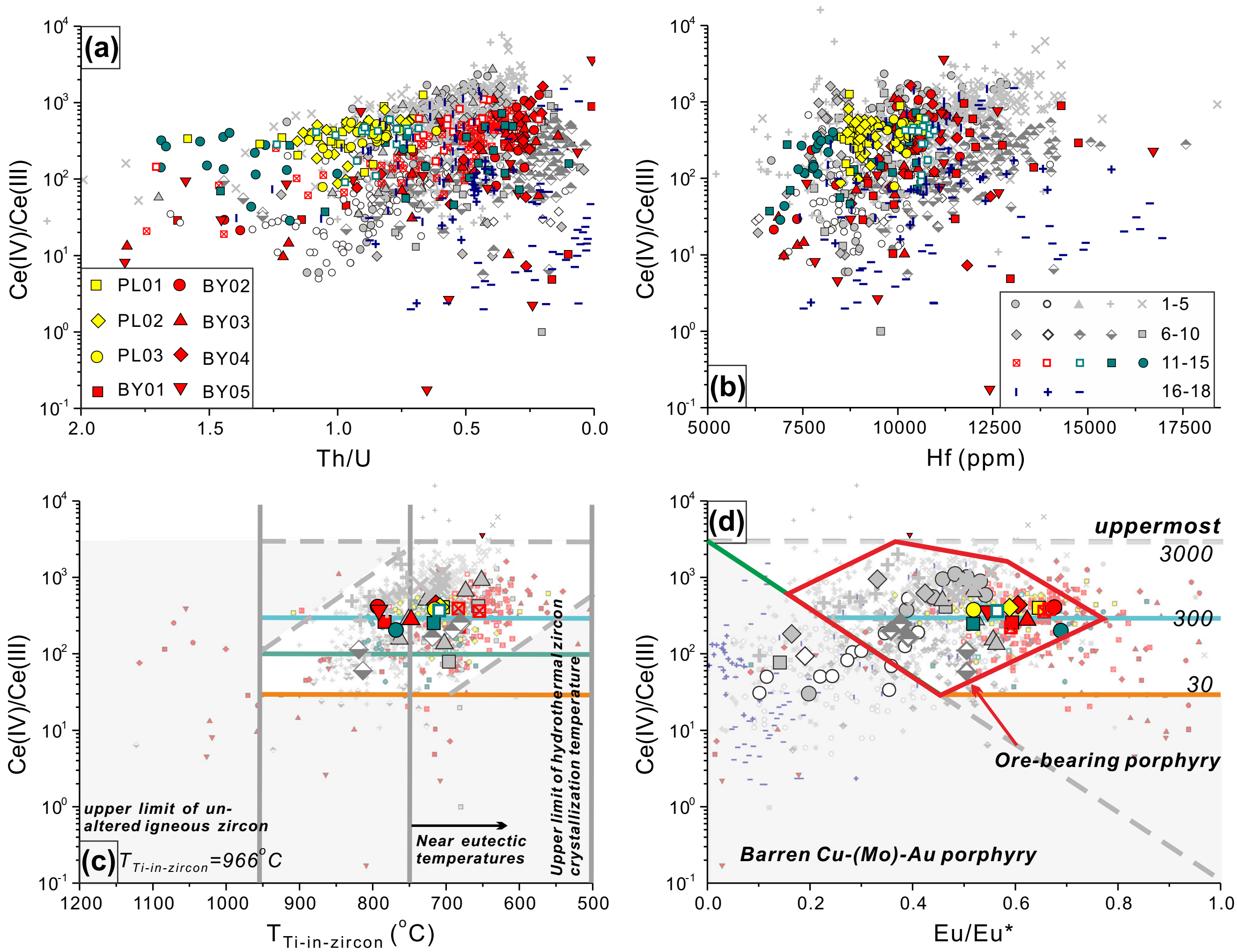

Fig. 10 Correlation between Ce^{IV}/Ce^{III} and (**a**) Th/U, (**b**) Hf, (**c**) T, and (**d**) Eu/Eu* values. The Ce^{IV}/Ce^{III} values are calculated by the lattice strain model (Ballard et al. 2002). The large symbols in Fig. 10d represent the average values of each samples. The boundary values of maximum Ti-in-zircon temperature of unaltered igneous zircon and hydrothermal zircons are following Hoskin and Schaltegger (2003) and Fu et al. (2009). Near eutectic temperatures are after Dilles et al., (2015). (1–2) Chuquicamata and El Abra Cu-fertile (1) and barren porphyries (2) in northern Chile (Ballard et al. 2002). (3) El Teniente Cu-Mo-fertile porphyries in central Chile (Muñoz et al. 2012). (4) Porphyries from Oyu Tolgoi Cu-Au district in southern Mongolia (Wainwright et al. 2011). (5) Quellaveco Cu-Mo-fertile porphyries in southern Peru (Simmons 2013). (6–7) Medet Cu-fertile (6) and barren porphyries (7) in Bulgaria (Peytcheva et al. 2009). (8) Battle Mountain Cu-Au-fertile porphyries and (9) Carlin Au-related porphyries in northern Nevada, USA (Farmer 2013). The porphyry rocks in China are from (10) Dabaoshan Mo-Cu (Li et al. 2012a), (11) Yulong Cu-Mo (Li et al. 2012b), (12) Machangqing Cu (Guo et al. 2011), and (13) Langdu Cu (Jin et al. 2013), (14) Hongniu skarn Cu deposit, and (15) Triassic Cu-fertile porphyry in Zhongdian arc. (16) I-type granite and (17) A-type ore-barren granite, and (18) S-type ore-barren granite in Tibet (Wang et al. 2012)

are best interpreted as the rejuvenation by hotter, younger, relatively reduced magmas of an initial oxidized magma pool. In contrast, the typical compositional zonation of zircons from the Pulang porphyries mimic simple cooling and chemical differentiation of the host magma (Ginibre et al. 2007).

The thermal and physical state of upper crustal magma chambers may be disrupted by the incremental injection of small magma pulses. The injection of external magma pulses revealed by reversal of chemical (e.g., Ti-in-zircon temperature, Ce^{IV}/Ce^{III}) zonation in zircon indicates mass and energy exchange between a magma body with its external environment (Streck 2008). In the Beiya district, the presence of Au-bearing granite porphyry dikes intruding the quartz monzonite porphyry stock (Deng et al. 2015) also supports multiple pulses from a deep magma chamber. The fluctuation of temperature and oxygen fugacity estimated from elemental variation of magnetites cystallized from the different stages of hydrothermal fluids in the Beiya deposits also indicates the introduction of younger melt into the pre-existing unconsolidated magma system (Sun et al. 2017). Hence, we believe that the zircon signature of the Beiya porphyries resulted from a mixing process in the upper crust.

Magmatic f_{O2} conditions for generating Cu-Au-bearing melts

A high magmatic fluid flux ensures the exsolution of an aqueous volatile phase, which is considered as the sine qua non for magmatic hydrothermal ore-forming systems (Richards 2011). The investigated Cu-Au-related porphyries commonly contain amphibole or biotite phenocrysts and are characterized by high Sr/Y and La/Yb ratios, as well as listric-shaped normalized REE patterns, which indicate high water content (Li et al. 2011; Lu et al. 2013). Another key issue in generating a magmatic hydrothermal Cu-Au deposit is the ability of magma to transport metals into the upper crust.

Magma generated at $f_{O2} \geq$ FMQ + 2 (Mungall 2002) or +2.3 (Jugo 2009) would preserve Cu and Au contents in silicate melts due to the instability of sulfide phases. The estimated oxygen fugacity using amphibole chemistry for the Pulang Cu porphyry is NNO + 2.8 (Liu et al. 2013). This result is consistent with the values calculated by zircon chemistry, implying a relatively oxidized magma for the porphyry. The determined zircon Ce^{IV}/Ce^{III} values are comparable to those of the Yulong and Machangqing Cu porphyries along the Jinshajiang belt, and the Dexing Cu porphyry in southeastern China (Fig. 10). Our samples also mostly fall close to those of the Chuquicamata-El Abra samples, indicating that the elevated redox state of these porphyry suites favors Cu mineralization.

The qualitative oxygen fugacities of other two adjacent post-collisional porphyry systems generated from 37 to 33 Ma in western Yunnan (i.e., the Machangqing porphyry Cu-Mo system and the Yao'an porphyry Au system) have ever been estimated through other methods (Bi et al. 2009).We re-use the data from Bi et al. (2009) to obtain estimated crystallization temperatures and redox states. The results show the Yao'an Au-fertile porphyry (820 °C, ~FMQ + 0.9) and Machangqing Cu-fertile porphyry (730 °C,~FMQ + 2.7) are also the products of oxidized magma, similar to the Pulang (~709 ± 6 °C, ~FMQ + 4.0 ± 1.0, $n = 3$) and Beiya porphyries (~780 ± 22 °C, ~FMQ + 1.9 ± 1.3, $n = 5$) within our defined error range. We thus propose that formation of Cu-Au-bearing porphyries requires elevated oxygen fugacities but varible temperatures.

Evaluating the economic potential of porphyry-related Cu-Au deposits

Magmatic oxidation state controls sulfur speciation and metal solubility in magmas (Hamlyn et al. 1985; Bornhorst and Rose 1986; Jugo 2004; Jugo 2009) and high magmatic water contents ensure exsolution of aqueous volatile phases. The Ce^{IV}/Ce^{III} ratio calculated through the lattice-strain model is a common indicator of magmatic oxidation state, and the $(Eu/Eu^*)_N$ ratio is instrumental in indicating either high oxidation state or magmatic water contents (Richards 2011; Ballard et al. 2002; Dilles et al. 2015). Ballard et al. (2002) examined fertile and barren porphyry stocks and showed that the productive porphyries exhibited relatively high ratios (Ce^{IV}/Ce^{III} > 300 and Eu_N/Eu_N^* > 0.4). However, the later published large amounts of data are not well explained in this discrimination diagram. Based on the compiled database, an optimal more constrained interval for Cu-Au porphyry formation is thus shown in Fig. 10c, d. Most zircons from the porphyries show Ce^{IV}/Ce^{III} values lower than 3000, and Eu/Eu^*_N less than 0.8, and crystallization temperatures ranging from 650 to 850 °C.

Conclusions

(1) In contrast to the Pulang Cu-fertile porphyry, the Beiya porphyries formed by at least two different melt pulses. Zircon geochemistry obtained by LA-ICP-MS can be used to estimate magma redox state. The calculated Ti-in-zircon temperatures and FMQ values of Pulang are 709 ± 6 °C and 4.0 ± 1.0 ($n = 3$), whereas those values for Beiya porphyries are 780 ± 22 °C and 1.9 ± 1.3 ($n = 5$), respectively.

(2) Combined with a compilation of published zircon data, an optimal interval on Ce^{IV}/Ce^{III}-$T_{Ti\text{-}in\text{-}zircon}$ and $(Eu/Eu^*)_N$ diagrams for producing magmatic hydrothermal Cu-Au deposits is identified. We foresee that the diagrams can help reduce risk at the first exploration step for porphyry Cu-Au deposits, therefore decreasing the economic and environmental cost.

Acknowledgements We express our appreciation to Mingyue Hu who provided in-kind analytical work for LA-ICP-MS zircon trace element analysis and Junting Qiu for his assistance in f_{O2} calculation through zircon trace elements. Careful reviews by Franco Pirajno and Jeremy Richards improved the quality of the initial version. The manuscript also benefited considerably from the constructive reviews from Bernd Lehmann, Ruizhong Hu, and two anonymous reviewers. All these contributions are kindly appreciated.

Funding This research was jointly supported by the Chinese Geological Survey (Project 12120113093700), National Natural Science Foundation of China (Grant Nos. 40902029), a 973 project of China (2014CB440903), Public Scientific Research (Project No. 200911007), the open research fund from the Key Laboratory of Metallogeny and Mineral Assessment (MLR), and by Yunnan Gold and Mineral Resources Corporation (Project: Metallogenic Regularity and Minerogenetic Series Research of Gold Polymetallic Deposits in West Yunnan Province, China).

References

Ballard JR, Palin JM, Campbell IH (2002) Relative oxidation states of magmas inferred from Ce(IV)/Ce(III) in zircon: application to porphyry copper deposits of northern Chile. Contrib Mineral Petrol 144:347–364. https://doi.org/10.1007/s00410-002-0402-5

Barnes HL (1979) Solubilities of ore minerals. Geochem Hydrothermal Ore Deposits 2:404–460

Bea F, Pereira MD, Stroh A (1994) Mineral/leucosome trace-element partitioning in a peraluminous migmatite (a laser ablation-ICP-MS study). Chem Geol 117:291–312

BGMRSP (1991) Regional geology of Yunnan Province. Geological Publishing House, Beijing **728 p**. (in Chinese with English abstract)

Bi XW, Hu RZ, Hanley JJ, Mungall JE, Peng JT, Shang LB, Wu KX, Suang Y, Li HL, Hu XY (2009) Crystallisation conditions (T, P, f_{O2}) from mineral chemistry of Cu- and Au-mineralised alkaline intrusions in the Red River-Jinshajiang alkaline igneous belt, western Yunnan Province, China. Mineral Petrol 96:43–58

Blevin PL, Chappell BW (1992) The role of magma sources, oxidation-states and fractionation in determining the granite metallogeny of Eastern Australia. T Roy Soc Edin-Earth 83:305–316

Bornhorst TJ, Rose WI (1986) Partitioning of gold in young calc-alkalic volcanic rocks from Guatemala. J Geol 94:412–418

Brett R, Sato M (1984) Intrinsic oxygen fugacity measurements on seven chondrites, a pallasite, and a tektite and the redox state of meteorite parent bodies. Geochim Cosmochim Acta 48:111–120

Buddington AF, Lindsley DH (1964) Iron-titanium oxide minerals and synthetic equivalents. J Petrol 5:310–357

Burnham CW (1980) Late-stage processes of felsic magmatism. Soc Mining Geol Jpn 8:1–11

Chang CF (1997) Geology and tectonics of Qinghai-Xizang Plateau. Science Press, Beijing **153 p.** (in Chinese with English abstract)

Chen BW, Wang KY, Liu WJ, Cai ZJ, Zhang QW, Peng XJ, Qiu YZ, Zheng YZ (1987) Geotectonics of the Nujiang-Langcangjiang-Jinshajiang Region. Geological Publishing House, Beijing **204 p.** (in Chinese with English abstract)

Cherniak DJ, Hanchar JM, Watson EB (1997) Diffusion of tetravalent cations in zircon. Contrib Mineral Petrol 127:383–390

Chou IM (1978) Calibration of oxygen buffers at elevated P and T using the hydrogen fugacity sensor. Am Mineral 63:690–703

Chung S-L, Chu M-F, Zhang Y, Xie Y, Lo C-H, Lee T-Y, Lan C-Y, Li X, Zhang Q, Wang Y (2005) Tibetan tectonic evolution inferred from spatial and temporal variations in post-collisional magmatism. Earth Sci Rev 68:173–196

Claiborne LL, Miller CF, Walker BA, Wooden JL, Mazdab FK, Bea F (2006) Tracking magmatic processes through Zr/Hf ratios in rocks and Hf and Ti zoning in zircons: an example from the Spirit Mountain batholith, Nevada. Mineral Mag 70:517–543

Claiborne LL, Miller CF, Wooden JL (2010) Trace element composition of igneous zircon: a thermal and compositional record of the accumulation and evolution of a large silicic batholith, Spirit Mountain, Nevada. Contrib Mineral Petrol 160:511–531

Deng J, Hou ZQ, Mo XX, Yang LQ, Wang QF, Wang CM (2010) Superimposed orogenesis and metallogenesis in Sanjiang Tethys. Mineral Deposits 29:37–42 (In Chinese with English Abstract)

Deng J, Wang QF, Li GJ, Hou ZQ, Jiang CZ, Danyushevsky L (2015) Geology and genesis of the giant Beiya porphyry–skarn gold deposit, northwestern Yangtze Block, China. Ore Geol Rev 70:457–485

Deng J, Wang QF, Li GJ, Li CS, Wang CM (2014) Tethys tectonic evolution and its bearing on the distribution of important mineral deposits in the Sanjiang region, SW China. Gondwana Res 26:419–437

Dilles JH, Kent AJR, Wooden JL, Tosdal RM, Koleszar A, Lee RG, Farmer LP (2015) Zircon compositional evidence for sulfur-degassing from ore-forming arc magma. Econ Geol 110:241–251

Eugster HP, Wones DR (1962) Stability relations of the ferruginous biotite, annite. J Petrol 3:82–125

Farmer LP (2013) Trace element characteristics of zircon: a means of assessing mineralization potential of intrusions in northern Nevada. Oregon State University, Corvallis **92 p**

Ferry JM, Watson EB (2007) New thermodynamic models and revised calibrations for the Ti-in-zircon and Zr-in-rutile thermometers. Contrib Mineral Petrol 154:429–437

Fu B, Mernagh TP, Kita NT, Kemp AIS, Valley JW (2009) Distinguishing magmatic zircon from hydrothermal zircon: a case study from the Gidginbung high sulphidation Au–Ag–(Cu) deposit, SE Australia. Chem Geol 259:131–142

Fujimaki H (1986) Partition coefficients of Hf, Zr, and REE between zircon, apatite, and liquid. Contrib Mineral Petrol 94:42–45

Ghiorso MS, Sack O (1991) Fe-Ti oxide geothermometry: thermodynamic formulation and the estimation of intensive variables in silicic magmas. Contrib Mineral Petrol 108:485–510

Ginibre C, Worner G, Kronz A (2007) Crystal zoning as an archive for magma evolution. Elements 3:261–266

Green TH (1994) Experimental studies of trace-element partitioning applicable to igneous petrogenesis—Sedona 16 years later. Chem Geol 117:1–36

Guo XD, Wang ZH, Wang L, Yang YX, Chen XW (2011) LA-ICP-MS zircon U-Pb ages of porphyritic granite in Machangqing complex of Yunnan Province and their geological significance. Geol China 38: 610–622 (In Chinese with English abstract)

Hamlyn PR, Keays RR, Cameron WE, Crawford AJ, Waldron HM (1985) Precious metals in magnesian low-Ti lavas: implications for metallogenesis and sulfur saturation in primary magmas. Geochim Cosmochim Acta 49:1797–1811

Hanchar JM, Van Westrenen W (2007) Rare earth element behavior in zircon-melt systems. Elements 3:37–42

He WY, Mo XX, He ZH, White NC, Chen JB, Yang KH, Wang R, XH Y, Dong GC, Huang XF (2015) The geology and mineralogy of the Beiya skarn gold deposit in Yunnan, southwest China. Econ Geol 110:1625–1641

He WY, Yang LQ, Brugger J, McCuaig TC, Lu YJ, Bao XS, Gao XQ, Lu YG, Xing YL (2016) Hydrothermal evolution and ore genesis of the Beiya giant Au polymetallic deposit, western Yunnan, China: Evidence from fluid inclusions and H–O–S–Pb isotopes. Ore Geol Rev. https://doi.org/10.1016/j.oregeorev.2016.10.035

Hedenquist JW, Lowenstern JB (1994) The role of magmas in the formation of hydrothermal ore-deposits. Nature 370:519–527

Hoskin PWO, Schaltegger U (2003) The composition of zircon and igneous and metamorphic petrogenesis. In: Hanchar JM, Hoskin PWO (eds) Zircon: reviews in mineralogy and geochemistry, 53. Mineralogical Society of America, Chantilly, pp 27–62

Hou ZQ, Yang YQ, Wang HP, Qu XM, Lv QT, Huang DH, Wu XZ, Yu JJ, Tang SH, Zhao JH (2003) Collision-orogenic progress and minerlization system of Yidun arc. Geological Publishing House, Beijing **335 p.** (in Chinese with English abstract)

Hu MY, Fan XT, Stoll B, Kuzmin D, Liu Y, Liu YS, Sun WD, Wang G, Zhan XC, Jochum KP (2011) Preliminary characterisation of new reference materials for microanalysis: Chinese Geological Standard Glasses CGSG-1, CGSG-2, CGSG-4 and CGSG-5. Geostand Geoanal Res 35:235–251

Hu RZ, Burnard PG, Bi XW, Zhou MF, Pen JT, WC S, KX W (2004) Helium and argon isotope geochemistry of alkaline intrusion-associated gold and copper deposits along the Red River–Jinshajiang fault belt, SW China. Chem Geol 203:305–317. https://doi.org/10.1016/j.chemgeo.2003.10.006

Huebner JS (1971) Buffering techniques for hydrostatic systems at elevated pressures. In Ulmer GC (ed) Research techniques for high pressure and high temperature. Springer-Verlag, New York, pp 123–177

Huebner JS, Sato M (1970) The oxygen fugacity-temperature relationships of manganese oxide and nickel oxide buffer. Am Mineral 55: 934–952

Jin CH, Fan WY, Zhang Y, Zhang H, Shen ZW, Gao JH (2013) Trace element composition and U-Pb chronology of zircons in monzonite porphyry from the Langdu copper deposit in Zhongdian and their geological significance. Geotecton Metallog 37:262–272 (in Chinese with English abstract)

Jugo PJ (2004) An experimental study of the sulfur content in basaltic melts saturated with immiscible sulfide or sulfate liquids at 1300 °C and 1.0 GPa. J Petrol 46:783–798

Jugo PJ (2009) Sulfur content at sulfide saturation in oxidized magmas. Geology 37:415–418

Jugo PJ, Luth RW, Richards JP (2005) Experimental data on the speciation of sulfur as a function of oxygen fugacity in basaltic melts. Geochim Cosmochim Acta 69:497–503

Lee RG (2008). Genesis of the El Salvador porphyry copper deposit, Chile and distribution of epithermal alteration at Lassen Peak, California (Doctoral dissertation)

Leloup PH, Kienast JR (1993) High-temperature metamorphism in a major strike-slip shear zone: the Ailao Shan—Red River, People's Republic of China. Earth Planet Sci Lett 118:213–234

Leloup PH, Lacassin R, Tapponnier P, Schärer U, Zhong DL, Liu XH, Zhang LS, Ji SC, Trinh PT (1995) The Ailao Shan-Red River shear zone (Yunnan, China), Tertiary transform boundary of Indochina. Tectonophysics 251:3–84

Lepage LD (2003) ILMAT: an Excel worksheet for ilmenite–magnetite geothermometry and geobarometry. Comput Geosci 29:673–678

Li CY, Zhang H, Wang FY, Liu JQ, Sun YL, Hao XL, Li YL, Sun WD (2012b) The formation of the Dabaoshan porphyry molybdenum deposit induced by slab rollback. Lithos 150:101–110

Li JX, Qin KZ, Li GM, Cao MJ, Xiao B, Chen L, Zhao JX, Evans NJ, McInnes BIA (2012a) Petrogenesis and thermal history of the Yulong porphyry copper deposit, Eastern Tibet: insights from U-Pb and U-Th/He dating, and zircon Hf isotope and trace element analysis. Mineral Petrol 105:201–221

Li WC, Zeng PS, Hou ZQ, NC W (2011) The Pulang porphyry copper deposit and association felsic intrusions in Yunnan province, southwest China. Econ Geol 106:79–92

Liang HY, Campbell IH, Allen CM, Sun WD, HX Y, Xie YW, Zhang YQ (2007) the age of the potassic alkaline igneous rocks along the Ailao Shan–Red River Shear Zone: implications for the onset age of left-lateral shearing. J Geol 115:231–242

Liu B, Liu H, Zhang CQ, Mao ZH, Zhou YM, Huang H, He ZH, GS S (2015a) Geochemistry and geochronology of porphyries from the Beiya gold–polymetallic orefield, western Yunnan, China. Ore Geol Rev 69:360–379

Liu H, Zhang CQ, Jia FD, Zhou YM, Lou DB (2015b) Mineral and geochemical evidences of magma-mixing from Pulang porphyry copper deposit in SW Sanjiang, China. Acta Petrol Sin 31:3189–3202 (in Chinese with English abstract)

Liu XL, Li WC, Yin GH, Zhang N (2013) The geochronology, mineralogy and geochemistry study of the Pulang porphyry copper deposits in Geza arc of Yunnan Province. Acta Petrol Sin 29:3094–3064 (in Chinese with English abstract)

Lu YJ, Kerrich R, Kemp AIS, McCuaig TC, Hou ZQ, Hart CJR, Li ZX, Cawood PA, Bagas L, Yang ZM, Cliff J, Belousova EA, Jourdan F, Evans NJ (2013) Intracontinental Eocene-Oligocene porphyry Cu mineral systems of Yunnan, Western Yangtze Craton, China: compositional characteristics, sources, and implications for continental collision metallogeny. Econ Geol 108:1541–1576

Luo MC, Wang LQ, Leng QF, Che W (2011) Zircon Hf isotope and Ce^{4+}/Ce^{3+} ratio of the monzogranite porphyry and biotite monzonitic granite in Bangpu Mo(Cu) deposit, Tibet. Mineral Deposits 30:266–278 (in Chinese with English abstract)

Luo Y, Ayers JC (2009) Experimental measurements of zircon/melt trace-element partition coefficients. Geochim Cosmochim Acta 73:3656–3679

Mao JW, Pirajno F, Lehmann B, Luo MC, Berzina A (2014) Distribution of porphyry deposits in the Eurasian continent and their corresponding tectonic settings. J Asian Earth Sci 79:576–584

Mao JW, Zhou YM, Liu H, Zhang CQ, DG F, Liu B (2017) Metallogenic setting and ore genetic model for the Beiya porphyry-skarn polymetallic Au orefield, western Yunnan, China. Ore Geol Rev 86:21–34

Metcalfe I (2006) Palaeozoic and Mesozoic tectonic evolution and palaeogeography of East Asian crustal fragments: the Korean Peninsula in context. Gondwana Res 9:24–46

Metcalfe I (2013) Gondwana dispersion and Asian accretion: tectonic and palaeogeographic evolution of eastern Tethys. J Asian Earth Sci 66:1–33

Mo XX, Lu FX, Shen SY, Zhu QW, Hou ZQ, Yang KH, Deng JF, Liu XP, He CX, Lin PY, Zhang BM, Tai DQ, Chen MH, Hu XS, Ye S, Xue YX, Tan J, Wei QR, Fan L (1993) Sanjiang Tethyan volcanism and related mineralization. Geological Publishing House, Beijing (in Chinese with English abstract)

Mungall JE (2002) Roasting the mantle: slab melting and the genesis of major Au and Au-rich Cu deposits. Geology 30:915–918

Muñoz M, Charrier R, Fanning CM, Maksaev V, Deckart K (2012) Zircon trace element and O–Hf isotope analyses of mineralized intrusions from El Teniente ore deposit, Chilean Andes: constraints on the source and magmatic evolution of porphyry Cu–Mo related magmas. J Petrol 53:1091–1122

Nardi LVS, Formoso MLL, Muller IF, Fontana E, Jarvis K, Lamarao C (2013) Zircon/rock partition coefficients of REEs, Y, Th, U, Nb, and Ta in granitic rocks: uses for provenance and mineral exploration purposes. Chem Geol 335:1–7

Pan GT, Xu Q, Hou ZQ, Wang LQ, Du DX, Mo XX, Li DM, Wang MJ, Li XZ, Jiang XS (2003) Archipelagic orogenesis, metallogenic systems and assessment of the mineral resources along the Nujiang-Lancangjiang-Jinshajiang area in southwestern China. Geological Publishing House, Beijing (in Chinese with English abstract)

Pang ZS, YS D, Wang GW, Guo X, Cao Y, Li Q (2009) Single-grain zircon U-Pb isotopic ages, geochemistry and its implication of the Pulang complex in Yunnan Province, China. Acta Petrol Sin 25:159–165

Peng HJ, Mao JW, Pei RF, Zhang CQ, Tian G, Zhou YM, Li JX, Hou L (2014) Geochronology of the Hongniu-Hongshan porphyry and skarn Cu deposit, northwestern Yunnan province, China: implications for mineralization of the Zhongdian arc. J Asian Earth Sci 79:682–695

Peytcheva I, von Quadt A, Neubauer F, Frank M, Nedialkov R, Heinrich C, Strashimirov S (2009) U–Pb dating, Hf-isotope characteristics and trace-REE-patterns of zircons from Medet porphyry copper deposit, Bulgaria: implications for timing, duration and sources of ore-bearing magmatism. Mineral Petrol 96:19–41

Richards JP (2011) High Sr/Y arc magmas and porphyry Cu ± Mo ± Au deposits: just add water. Econ Geol 106:1075–1081

Ridolfi F, Renzulli A (2012) Calcic amphiboles in calc-alkaline and alkaline magmas: thermobarometric and chemometric empirical equations valid up to 1,130 °C and 2.2 GPa. Contri Mineral Petrol 163:877–895

Ridolfi F, Renzulli A, Puerini M (2010) Stability and chemical equilibrium of amphibole in calc-alkaline magmas: an overview, new thermobarometric formulations and application to subduction-related volcanoes. Contri Mineral Petrol 160:45–66

Rubatto D, Hermann J (2007) Experimental zircon/melt and zircon/garnet trace element partitioning and implications for the geochronology of crustal rocks. Chem Geol 241:38–61

Sano Y, Terada K, Fukuoka T (2002) High mass resolution ion microprobe analysis of rare earth elements in silicate glass, apatite and zircon: lack of matrix dependency. Chem Geol 184:217–230

Scaillet B, Evans BW (1999) The 15 June 1991 eruption of Mount Pinatubo. I. Phase equilibria and pre-eruption P–T–f_{O2}–f_{H2O} conditions of the dacite magma. J Petrol 40:381–411

Sha SL (1998) Glaucophane schist in the conjunction of Zhongdian, Yunann and Muli, Sichuan (Louji-Wachang). Yunnan Geol 7:82–85 (in Chinese with English abstract)

Soloview SG (2015) Geology, mineralization, and fluid inclusion characteristics of the Kumbel oxidized W–Cu–Mo skarn and Au–W stockwork deposit in Kyrgyzstan, Tien Shan. Mineral Deposits 50: 187–220

Streck MJ (2008) Mineral textures and zoning as evidence for open system processes. Rev Mineral Geochem 69:595–622

Sun SS, McDonough WF (1989) Chemical and isotopic systematics of oceanic basalts: implications for mantle composition and processes. Geol Soc Lond, Spec Publ 42:313–345

Sun XM, Lin H, Fu Y, Li DF, Hollings P, Yang TJ, Liu ZG (2017) Trace element geochemistry of magnetite from the giant Beiya gold-polymetallic deposit in Yunnan Province, Southwest China and its implications for the ore forming processes. Ore Geol Rev. https://doi.org/10.1016/j.oregeorev.2017.09.007.

Tapponnier P, Lacassin R, Leloup PH, Schärer U, Zhong Dl WHW, Liu XH, Ji SC, Zhang LS, Zhong JY (1990) The Ailao Shan/Red River metamorphic belt: Tertiary left-lateral shear between Indochina and south China. Nature 343(6257):431

Tran MD, Liu JL, Nguyen QL, Chen Y, Tang Y, Song ZJ, Zhang ZC, Zhao ZD (2014) Cenozoic high-K alkaline magmatism and associated Cu-Mo-Au mineralization in the Jinping-Fan Si Pan region, southeastern Ailao Shan-Red River shear zone, southwestern China-northwestern Vietnam. J Asian Earth Sci 79:858–872

Turner S, Arnaud N, Liu J, Rogers N, Hawkesworth C, Harris N, Kelley S, van Calsteren P, Deng WM (1996) Postcollisional, shoshonitic volcanism on the Tibetan Plateau: implications for convective thinning of the lithosphere and the source of ocean island basalts. J Petrol 37:45–71

Wainwright AJ, Tosdal RM, Wooden JL, Mazdab FK, Friedman RM (2011) U–Pb (zircon) and geochemical constraints on the age, origin, and evolution of Paleozoic arc magmas in the Oyu Tolgoi porphyry Cu–Au district, southern Mongolia. Gondwana Res 19:764–787

Wang BD, Wang LQ, Chen JL, Yin FG, Wang DB, Zhang WP, Chen LK, Liu H (2014b) Triassic three-stage collision in the Paleo-Tethys: constraints from magmatism in the Jiangda–Deqen–Weixi continental margin arc, SW China. Gondwana Res 26:475–491

Wang JH, Yin A, Harrison TM, Grove M, Zhang YQ, Xie GH (2001) A tectonic model for Cenozoic igneous activities in the eastern Indo–Asian collision zone. Earth Planet Sci Lett 188:123–133

Wang Q, Zhu DC, Zhao ZD, Guan Q, Zhang XQ, Sui QL, ZC H, Mo XX (2012) Magmatic zircons from I-, S- and A-type granitoids in Tibet: trace element characteristics and their application to detrital zircon provenance study. J Asian Earth Sci 53:59–66

Wang SX, Zhang XC, Leng CB, Qin CJ, Ma DY, Wang WQ (2008) Zircon SHRIMP U-Pb dating of the Pulang porphyry copper deposit, northwestern Yunan, China: the ore-forming time limitation and geological significance. Acta Petrol Sin 24:2313–2321

Wang XS, Bi XW, Leng CB, Zhong H, Tang HF, Chen YW, Yin GH, Huang DZ, Zhou MF (2014a) Geochronology and geochemistry of Late Cretaceous igneous intrusions and Mo–Cu–(W) mineralization in the southern Yidun Arc, SW China: implications for metallogenesis and geodynamic setting. Ore Geol Rev 61:73–95

Watson EB (1996) Dissolution, growth and survival of zircons during crustal fusion: kinetic principles, geological models and implications for isotopic inheritance. T Roy Soc Edin-Earth 87:43–56

Xin HB, Qu XM (2008) Relative oxidation states of Ore-bearing porphyries inferred from Ce(IV)/Ce(III) ratio in zircon: application to the porphyry copper belt at Gangdese, Tibet. Acta Mineral Sin 28:152–160 (in Chinese with English abstract)

Xu XW, Cai XP, Xiao QB, Peters SG (2007) Porphyry Cu–Au and associated polymetallic Fe–Cu–Au deposits in the Beiya Area, western Yunnan Province, south China. Ore Geol Rev 31:224–246

Xu YG, Chung SL, Jahn BM, GY W (2001) Petrologic and geochemical constraints on the petrogenesis of Permian–Triassic Emeishan flood basalts in southwestern China. Lithos 58:145–168

Yang LQ, Deng J, Dilek Y, Meng JY, Gao X, Santosh M, Wang D, Yan H (2015) Melt source and evolution of I-type granitoids in the SE Tibetan Plateau: Late Cretaceous magmatism and mineralization driven by collision-induced transtensional tectonics. Lithos 245: 258–273

Yin A, Harrison TM (2000) Geologic evolution of the Himalayan-Tibetan orogen. Annu Rev Earth Planet Sci 28:211–280

Yunnan Gold & Mineral Group Co. L (2011) Reserves verification report of Beiya iron-gold deposit, Heqing. Yunnan Province. Yunnan Gold & Mineral Group Co., Ltd., Kunming (in Chinese with English abstract)

Zeng PS, Wang HP, Mo XX, Yu X, Li W (2004) Tectonic setting and prospects of porphyry copper deposits in Zhongdian island-arc belt. Acta Geosci Sin 25:535–540 (in Chinese with English abstract)

Zhang YQ, Xie YW, Tu GZ (1987) Preliminary studies of the alkali-rich intrusive rocks in the Ailaoshan-Jinshajiang belt and their bearing on rift tectonics. Acta Petrol Sin 1:17–26

Zhu JJ, RZ H, Richards JP, Bi XW, Zhong H (2015) Genesis and magmatic-hydrothermal evolution of the Yangla skarn Cu deposit, southwest China. Econ Geol 110:631–652

Zi JW, Cawood PA, Fan WM, Tohver E, Wang YJ, McCuaig TC (2012) Generation of early Indosinian enriched mantle-derived granitoid pluton in the Sanjiang Orogen (SW China) in response to closure of the Paleo-Tethys. Lithos 140:166–182